https://doi.org/10.5194/mr-2021-40
Preprint. Discussion started: 3 May 2021

Open Access MAGNETIC RESONANCE Discussions

Rapid Scan Electron Paramagnetic Resonance using an EPR-on-a-Chip Sensor

Silvio Künstner[1], Anh Chu[2], Klaus-Peter Dinse[1,5], Alexander Schnegg[3], Joseph E. McPeak[1], Boris Naydenov[1], Jens Anders[2,4], Klaus Lips[1,5]

[1]Berlin Joint EPR Laboratory and EPR4Energy, Department Spins in Energy Conversion and Quantum Information Science (ASPIN), Helmholtz-Zentrum Berlin für Materialien und Energie GmbH, Hahn-Meitner-Platz 1, 14109 Berlin, Germany
[2]Institute of Smart Sensors, Universität Stuttgart, 70569 Stuttgart, Germany
[3]EPR4Energy, Max-Planck-Institut für chemische Energiekonversion, 45470 Mülheim an der Ruhr, Germany
[4]Center for Integrated Quantum Science and Technology (IQST), Stuttgart and Ulm, Germany
[5]Berlin Joint EPR Laboratory, Fachbereich Physik, Freie Universität Berlin, 14195 Berlin, Germany

Correspondence to: Boris Naydenov (boris.naydenov@helmholtz-berlin.de)

Abstract. Electron paramagnetic resonance (EPR) spectroscopy is the method of choice to investigate and quantify paramagnetic species in many scientific fields, including materials science and the life sciences. Common EPR spectrometers use electromagnets and microwave (MW) resonators, limiting their application to dedicated lab environments. Here, we present an improved design of a miniaturized EPR spectrometer implemented on a silicon microchip (EPR-on-a-chip, EPRoC). In place of a microwave resonator, EPRoC uses an array of injection-locked voltage-controlled oscillators (VCOs), each incorporating a 200 µm diameter coil, as a combined microwave source and detector. The individual miniaturized VCO elements provide an excellent spin sensitivity reported to be about $4 \times 10^9 \mathrm{spins}/\sqrt{\mathrm{Hz}}$, which is extended by the array over a larger area for improved concentration sensitivity. A striking advantage of this design is the possibility to sweep the MW frequency instead of the magnetic field, which allows the use of smaller, permanent magnets instead of the bulky and power-hungry electromagnets required for field-swept EPR. Here, we report rapid scan EPR (RS-EPRoC) experiments performed by sweeping the frequency of the EPRoC VCO array. RS-EPRoC spectra demonstrate an improved SNR by approximately two orders of magnitude for similar signal acquisition times compared to continuous wave (CW-EPRoC) methods, which may improve the absolute spin and concentration sensitivity of EPR-on-a-Chip at 14 GHz to about 6×10^7 $\mathrm{spins}/\sqrt{\mathrm{Hz}}$ and $3.6\ \mathrm{nM}/\sqrt{\mathrm{Hz}}$, respectively.

1 Introduction

Electron Paramagnetic Resonance (EPR) spectroscopy is a widespread analytical tool for studying species with unpaired electrons relevant in chemistry, physics, biology, and medicine. The main uses of EPR are the quantification of paramagnetic centers (Eaton et al., 2010) in, e.g., chemical analyses or quality control, the identification and characterization of radicals (Villamena, 2017), paramagnetic defects (Brodsky and Title, 1969), and transition metal ion states (Van Doorslaer and Vinck, 2007) in biological samples, semiconductors, and during chemical reactions for assignment of the electronic and atomic structure of paramagnetic states (Neese, 2017).

In conventional EPR spectrometers, a microwave (MW) cavity resonator with a high quality factor (Q) is used to enhance the signal-to-noise ratio (SNR) and the resolution. The resonator couples the magnetic field component of the MW (~9.4 GHz in X-band spectrometers) to the magnetic moments of the unpaired electron spins of the sample. The response of the magnetic susceptibility of the sample is detected via the reflected MW using an MW bridge. To achieve the resonance condition, an external magnetic field, B_0, is swept linearly and continuously while the MW frequency is kept constant due to the very low bandwidth of the resonator, as dictated by the high Q employed to increase SNR. In standard continuous wave (CW, CW-EPR) operation, the magnetic field is modulated, allowing lock-in detection. Presently, EPR spectrometers are relatively bulky, having typical dimensions ranging from several tens of cm for smaller benchtop X-band systems to several meters for higher

https://doi.org/10.5194/mr-2021-40
Preprint. Discussion started: 3 May 2021

Open Access MAGNETIC RESONANCE Discussions

resolution research spectrometers. While the formers are limited to X-band operation, high-end spectrometers cover a much larger frequency range, operating at X- (9 GHz), Q- (36 GHz), W- (94 GHz) bands up to even higher frequencies (~263 GHz). Sales prices of EPR spectrometers range from ≈50 T€ for benchtop devices up to well over 1 M€ for high-end spectrometers. However, for a more widespread use of this powerful technique in science, industry, and even consumer applications, access to portable, cost-effective, and easy-to-operate EPR sensors is required. In the optimum case, such a spectrometer would consist of a single sensor that can be immersed in, attached to, or embedded in a sample of interest, removing the limitations of current resonator-based techniques. This vision requires a complete redesign of the EPR spectrometer, in whicc the bulky electromagnets and microwave parts are replaced by smaller permanent magnets and miniaturized electronic components capable of sweeping the frequency at a fixed magnetic field.

In pursuit of this redesign, EPR spectrometers have been developed to enable more flexible *operando* applications such as a hand-held EPR system (Wolfson et al., 2015) for transcutaneous oximetry, an EPR "dipstick" (Zgadzai et al., 2018) spectrometer that can be immersed in an aqueous solution, and the EPR Mobile Universal Surface Explorer (EPR-MOUSE) (Switala et al., 2017) as a field-swept, surface-sensitive EPR spectrometer. In all of these designs, however, a common microwave bridge is used for the MW generation and detection, limiting their applicability to dedicated laboratories.

Significant progress in semiconductor fabrication technology has propelled the design of new EPR spectrometers that are fully integrated into a single silicon microchip, so-called EPR-on-a-Chip (EPRoC) devices (Yalçin and Boero, 2008; Anders et al., 2012a). Such EPRoC devices use a voltage-controlled oscillator (VCO) via an embedded, miniaturized coil with a diameter of a few hundred micrometers both as microwave source and EPR detector. The idea of using a VCO instead of a microwave bridge to excite and detect the nuclear magnetic resonance (NMR) signal was first proposed in 1950 (Pound and Knight, 1950). Importantly, this approach breaks the classical trade-off between the resonator Q and detection sensitivity (Hyde et al., 2010), enabling frequency-swept EPR over wide frequency ranges with near-constant sensitivity. This allows the use of permanent magnets for smaller, more affordable, battery-driven spectrometers, as recently demonstrated (Schlecker et al., 2017a, b; Anders and Lips, 2019). The magnetic field strengths of practical permanent magnets (<1.5 T) limit the EPR resonance frequency to below 35 GHz; however, EPRoC detectors are much easier to integrate into complex and application-specific sample environments, opening the door to numerous potential in situ and/or operando EPR applications from room temperature to cryogenic temperatures down to 4 K (Gualco et al., 2014).

To further increase the sensitivity of the EPR technique, especially for samples with long relaxation times, the rapid scan EPR (RS-EPR) technique has been introduced (Eaton and Eaton, 2016). The advantage of the RS technique as compared to CW EPR is that much higher microwave excitation fields (B_1) can be used, which overcomes MW saturation limitations of the spin system by spending less time on resonance. Thereby, the SNR can be significantly enhanced in comparison to traditional CW-EPR (Eaton and Eaton, 2016). This is accomplished by scanning the magnetic field or MW frequency so quickly such that the resonance is passed in a time shorter than the relaxation times times T_1 and T_2^*. The EPR signal is recorded with a transient digitizer instead of a phase-sensitive detector, and passage effects may appear as "wiggles" on the trailing edge of the EPR resonance signals in the time domain. The passage effects can then be removed by *Fourier* deconvolution to recover the conventional slow-passage EPR spectrum (Joshi et al., 2005b; Tseitlin et al., 2011a). There are various reports on enhanced SNR of RS-EPR compared to CW-EPR using spin-trapped radicals (Mitchell et al., 2013a), nitroxyl radicals (Mitchell et al., 2012), irradiated fused quartz (Mitchell et al., 2011a), and samples with long relaxation rates such as hydrogenated amorphous silicon (a-Si:H) (Mitchell et al., 2013b; Möser et al., 2017) where the latter showed an improvement in spin sensitivity of more than one order of magnitude. In addition, RS-EPR allows for the determination of spin relaxation times, which is particularly useful in very high frequency EPR and under conditions where pulse EPR techniques are not applicable (Laguta et al., 2018). In most of the aforementioned experiments, field-swept RS-EPR was employed. Sweeping magnetic fields at high rates over a wide range is technically demanding and requires specialized coils and high current, high slew rate amplifiers. The realistically achievable maximum sweep width is limited to about 20 mT at slow rates (tens of kHz), restricting field-swept

https://doi.org/10.5194/mr-2021-40
Preprint. Discussion started: 3 May 2021

Open Access MAGNETIC RESONANCE Discussions

RS-EPR to the quite narrow spectra of the aforementioned sample classes (organic radicals, samples with low g anisotropy and small hyperfine interaction, etc.). Many transition metal ion states in biological and other samples, however, have much larger spectral widths. For faster rates, the sweep width is limited even more for typical resonator sample sizes. Additionally, vibrations of the coils and eddy currents induced in the metallic parts of the resonator may distort the spectrum, which may be especially large for fast, wide sweeps (Joshi et al., 2005a). The sweep width limitation of field-swept RS-EPR can be overcome using the non-adiabatic rapid sweep (NARS) (Kittell et al., 2011) or field-stepped direct detection (FSDD) EPR technique (Yu et al., 2015). This technique, however, complicates the data acquisition as well as the post-processing, prolongs the measurement time and necessitates the use of an electromagnet. Employing frequency-swept RS-EPR circumvents these problems, however, routinely used high Q, low bandwidth resonators limit the achievable sweep width considerably. With EPRoC, it is possible to utilize frequency-swept RS-EPR over large sweep widths of more than 1.8 GHz (63 mT) (Chu et al., 2017) without the constraints of resonator-based RS-EPR and thus may be used for interrogation of g and A anisotropy of samples with large hyperfine splitting and long relaxation times, such as in transition metal complexes at cryogenic temperatures, with increased sensitivity compared to CW-EPR using a small-footprint EPRoC spectrometer with a permanent magnet.

Here we report frequency-swept RS-EPR experiments (Tseitlin et al., 2011b) using an RS-EPRoC detector with an improvement of almost two orders of magnitude in SNR compared to CW-EPRoC measurements.

2 Materials and methods

2.1 EPR-on-a-Chip setup

The schematic of the employed experimental setup is depicted in Fig. 1. The EPRoC detector is located on a printed circuit board (PCB) which is inserted between the poles of an electromagnet (*Bruker* B-E 25) (Fig. 1a). The electromagnet was used solely because of immediate availability, without using the sweeping capabilities, and, in principle, a permanent magnet with sufficient homogeneity (<10 ppm) can be used instead. An EPRoC design with an array of twelve injection-locked VCOs was used (see Fig. 1c), similar to the design in Chu et al. (2018). Importantly, the injection locking of N VCOs lowers the phase noise of the joint array frequency by $\sqrt{N}$ (Chu et al., 2018). The utilized EPRoC detector has a frequency sweep range extending from 12.0 to 14.4 GHz (sweep width 2.4 GHz or 85.6 mT). In the experiments performed in this paper, we focus on the amplitude detection mode of the VCO-based detector, in which the EPR signal is measured as a change in the oscillation amplitude of the VCO (Chu et al., 2017). As discussed in Chu et al. (2017), an implicit wideband AM demodulation can be performed by current biasing the inductor-capacitor (LC) tank VCO. This scheme is implemented in one VCO inside the injection-locked VCO array, which is used as the EPR detector for all EPR experiments shown in this paper, cf. Fig. 1. The MW frequency of the EPRoC array is controlled by a phase-locked loop (PLL) with a bandwidth of about 10 MHz and a radio frequency (RF) generator (*Rohde & Schwarz* SMB100A) as the PLL frequency reference.

The B_1 magnitude may be varied by controlling the applied bias current, I_{bias}, to the VCO. All EPR measurements were performed as a frequency swept experiment with the EPRoC detector at a central microwave frequency of 13.44 GHz and at an external magnetic field of $B_0 = 479.4$ mT. For CW-EPRoC detection, sinusoidal frequency modulation is applied to the MW carrier wave with a modulation rate f_{m} and a peak-to-peak modulation amplitude $\Delta f_{\mathrm{m,pp}} = 2\Delta f_{\mathrm{m}}$ (see Eq. (6), below). The CW-EPRoC signal is detected with a lock-in amplifier (*Anfatec* eLockIn 203) and is linearly baseline-corrected using the outermost 5% of the recorded spectrum where no signal is present. A single grain of a α,γ-Bisdiphenylene-β-phenylallyl (BDPA, 1:1 with benzene from Sigma Aldrich, ~1.6 µg) was placed in the AM1 coil of the EPRoC detector (see Fig. 1c). The sample volume was calculated to be $6.7\text{x}10^{-4}$ mm^3 (0.67 nL) (for more information, see Appendix). BDPA gives an EPR signal at g = 2.003 with a linewidth of about 0.07 mT (Meyer et al., 2014).

https://doi.org/10.5194/mr-2021-40
Preprint. Discussion started: 3 May 2021

Open Access MAGNETIC RESONANCE Discussions

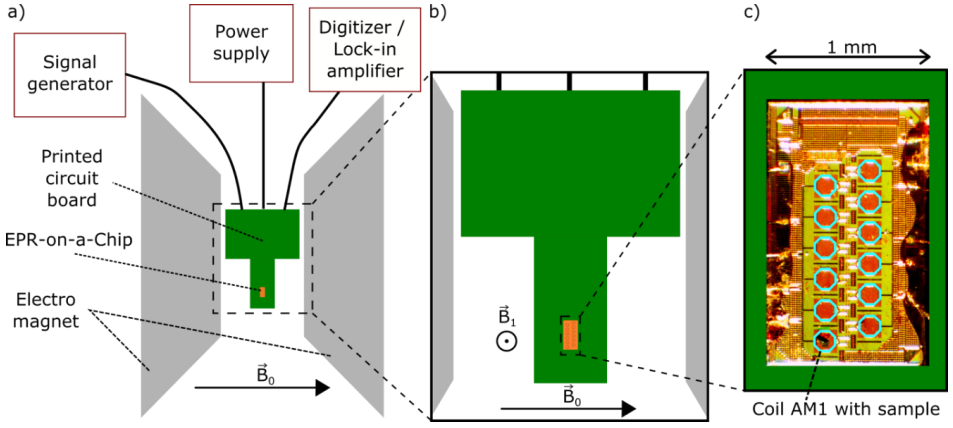

Figure 1: a) Depiction of the EPRoC setup. The EPRoC is located on the PCB which is inserted between the poles of the electromagnet. It is connected to a signal generator, a power supply and either a lock-in amplifier (LIA) for CW measurements or digitizer for RS operation. b) Close-up of the PCB. The directions of the static B_0 field and B_1 MW field are indicated by the arrows. c) Close-up of the EPRoC array with the twelve octagonal coils. The BDPA sample is placed in the coil AM1, where an AM signal can be detected.

Two techniques may be used for detecting the spin response with the EPRoC, namely amplitude-sensitive detection (AM) (Matheoud et al., 2018; Chu et al., 2021) and frequency-sensitive detection (FM) (Yalçin and Boero, 2008; Anders et al., 2012a). The AM and FM signals correspond to the EPR-induced changes in the VCO amplitude and frequency, respectively. While the FM signal purely represents the real component of the complex susceptibility, the AM signal represents a mixture of the imaginary, $\chi"$, and real, χ', components of the magnetic susceptibility (Chu et al., 2021). More specifically, the EPR-induced frequency changes, $\Delta\omega_{\mathrm{osc}}$, and amplitude changes, ΔA_{osc}, in the AM and FM detection modes can be written as:

$$\Delta A_{\mathrm{osc}} \propto Q\chi" - \chi' \tag{1}$$

$$\Delta\omega_{\mathrm{osc}} \propto \chi', \tag{2}$$

where Q is the quality factor of the LC tank inside the VCO. Note that the FM signal only depends on χ' (Eq. (2)) and that, depending on the quality factor at hand, the AM signal is primarily observed as an absorption signal according to $\chi"$, which is slightly distorted by the dispersion signal χ'. As mentioned above, for the measurements reported in this paper, only the AM signal was considered due to the large demodulation bandwidth of the implicit AM demodulator. This greatly facilitates AM RS-EPR experiments using EPRoC detectors compared to FM RS-EPRoC, where a much larger demodulation bandwidth is needed to demodulate the FM RS-EPR signal than is available in the current EPRoC (See Appendix for more information). For RS-EPRoC measurements, a complex transient signal was constructed from the AM signal by invoking the *Kramers-Kronig*[1] relationship to allow accurate deconvolution and reconstruction of the EPR spectrum.

2.3 Rapid scan using EPRoC

In RS-EPRoC operation, sinusoidal frequency modulation is applied to the fixed MW frequency, similar to CW-EPRoC operation; however, in the case of RS-EPRoC, much larger modulation rates, f_{m}, and frequency deviations, Δf_{m}, are used with the transient response detected directly and without lock-in amplification. The RS-EPRoC signal is recorded using a transient digitizer (*Zurich Instruments* UHF-LIA) with a sampling rate set to 450 MHz. For the baseline correction of the transient RS signal, a non-resonant transient RS background signal was recorded at a magnetic field of 400 mT and was subsequently subtracted from the experimental transient RS-EPRoC signal.

[1] Corresponding to a Hilbert transform of the signal.

https://doi.org/10.5194/mr-2021-40
Preprint. Discussion started: 3 May 2021

Open Access MAGNETIC RESONANCE Discussions

To ensure operation in the rapid passage regime as defined by Weger (1960), the scan rate α_{rot} of the MW frequency $\omega_{\mathrm{mw}} = 2\pi f_{\mathrm{mw}}$ must fulfill the following condition,

$$\alpha_{\mathrm{rot}} = \frac{\mathrm{d}\omega_{\mathrm{mw}}}{\mathrm{d}t} \gg \frac{|\gamma| B_1}{\sqrt{T_1 T_2}} \tag{3}$$

where γ is the gyromagnetic ratio of the spin, and B_1 is the amplitude of the MW excitation field. The criterion for a frequency sweep to reach the non-adiabatic rapid passage regime as defined by Powles (1958) only depends on B_1 according to

$$\frac{\mathrm{d}\omega_{\mathrm{mw}}}{\mathrm{d}t} \gg \gamma^2 B_1^2. \tag{4}$$

For sinusoidal frequency sweeps, which are used in all RS-EPRoC experiments reported in this paper, the excess[2] instantaneous microwave frequency, f_{i}, is defined as

$$f_{\mathrm{i}} = \Delta f_{\mathrm{m}} \cos(2\pi f_{\mathrm{m}} \tau), \tag{5}$$

where Δf_{m} is the modulation amplitude in Hz and f_{m} is the modulation frequency in Hz. In one scan period T, resonance is achieved twice, namely at $\tau = T/4$ and at $\tau = 3T/4$ where the scan rate, α, reaches a maximum

$$\alpha = \frac{\alpha_{\mathrm{rot}}}{2\pi} = \left.\frac{\mathrm{d}f_i}{\mathrm{d}t}\right|_{\mathrm{max}} = 2\pi f_{\mathrm{m}} \Delta f_{\mathrm{m}} \tag{6}$$

The maximum sweep width in these experiments was limited by the RF generator to $\Delta f_{\mathrm{m}} = 64$ MHz (4.57 mT) at modulation frequencies of up to 1 MHz; thus only about 5% of the available frequency sweep range of the EPRoC of about 2.4 GHz ($\Delta f_{\mathrm{m}} \approx 1.2$ GHz, sweep width 85.6 mT) was used. This in turn limited the maximum scan rate, α, to 402.1 THz/s, corresponding to 14.4 kT/s.

3 Results and discussion

3.1 Comparison between CW- and RS-EPRoC spectra

An example transient RS-EPRoC signal recorded with a bias current of 7 mA and a scan rate of 80 THz/s is depicted in Fig. 2a where the characteristic "wiggles" resulting from the non-adiabatic rapid passage are clearly observed. To recover the EPR spectrum, the transient RS-EPRoC signal is *Fourier* deconvolved from the sinusoidally oscillating MW excitation, as explained in detail in the Appendix. Only the imaginary component of the deconvolved RS-EPRoC spectrum, which corresponds to the imaginary component of the magnetic susceptibility, is shown in Fig. 2b. The CW spectrum of the same sample recorded using a bias current of 5 mA ($B_1 = 27$ µT) is also shown. The different bias currents in the two experiments were chosen to ensure operation in the linear regime, i.e., without microwave saturation.

As expected from Eq. (1), the CW-EPRoC signal exhibits an asymmetric line shape. There is no asymmetry in the RS-EPRoC spectrum because the complex RS-EPRoC spectrum can be phase-adjusted such that only the absorption signal is visible. In CW-EPRoC measurements, quadrature detection is not possible, and *Kramers-Kronig* manipulation is ill-suited due to slight signal saturation. Both spectra in Fig. 2b were simulated using the “pepper” function of the *Easyspin* software package (Stoll and Schweiger, 2006) assuming a spin-1/2 system with *Lorentzian* broadening. The asymmetry of the line shape in the CW spectrum is included in the simulation via a tailored fitting function according to Eq. (1), using a mixture of absorption and dispersion. A detailed description of the simulations is given in the Appendix.

[2] i.e in excess of the MW carrier frequency ω_{mw}

https://doi.org/10.5194/mr-2021-40
Preprint. Discussion started: 3 May 2021

Open Access MAGNETIC RESONANCE Discussions

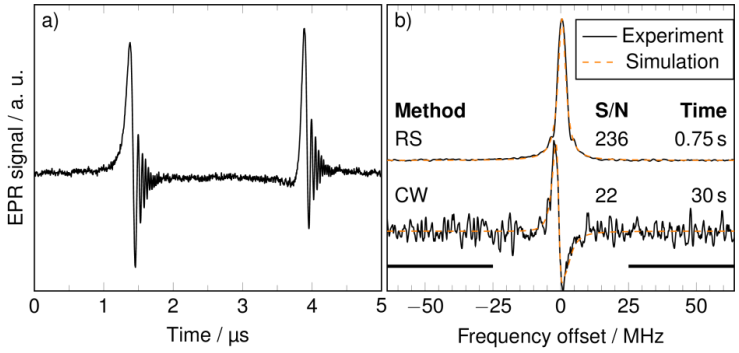

Figure 2: a) The background-corrected RS-EPRoC time trace recorded at a scan rate of 80 THz/s (2.9 kT/s; $\Delta f_m = 64$ MHz, $f_m = 200$ kHz, $I_{bias} = 7$ mA ($B_1 = 46$ µT)). b) Experimental data (black) and simulations (orange) of the CW ($I_{bias} = 5$ mA ($B_1 = 27$ µT)) and the deconvolved RS spectra.

The SNR and relevant parameters of CW- and RS-EPRoC measurements are summarized in Table 1. While only the imaginary component of the deconvolved spectrum is shown in Fig. 2, the SNR can in principle be further increased by a factor of $\sqrt{2}$ by the addition of the real and imaginary components of the RS-EPRoC spectrum (Tseitlin et al., 2010). Because the *Kramers-Kronig* relation is needed to obtain the complex transient RS-EPRoC signal in the presented setup, addition of both components of the spectrum following deconvolution is not valid due to noise correlation in the individual component spectra. The use of quadrature detection eliminates noise correlation and allows the real and imaginary components to be combined, increasing SNR similar to increasing the number of averages in the collected spectrum. RS-EPRoC measurements yield improved SNR when taking the much shorter measurement time for the RS-EPRoC spectrum into account, and an overall improvement in SNR of nearly two orders of magnitude is obtained in a given measurement time. For CW-EPRoC at 14 GHz, the absolute spin sensitivity was determined to be 4×10^9 spins/$\sqrt{\text{Hz}}$ using the FM EPRoC spectrum of BDPA (Handwerker et al., 2016). The concentration sensitivity may be calculated as the ratio of the absolute spin sensitivity and the active volume of the EPRoC (~27 nl) and is about 0.25 µM/$\sqrt{\text{Hz}}$ for CW-EPRoC. Since the theoretically achievable spin sensitivity of FM- and AM-detection with EPRoC is the same (Anders et al., 2012b; Chu et al., 2021), it is reasonable to combine this result with the SNR gain obtained here. Hence, we expect the same improvement of the absolute spin and concentration sensitivity, thus approximately 6×10^7 spins/$\sqrt{\text{Hz}}$ and 3.6 nM/$\sqrt{\text{Hz}}$ for RS-EPRoC, respectively. These results are in good agreement with those reported for field-swept RS-EPR of various sample classes, including nitroxyl radicals (Mitchell et al., 2012), irradiated fused quartz (Mitchell et al., 2011a), and samples with long relaxation times such as a-Si:H or N@C_{60} (Mitchell et al., 2013b; Möser et al., 2017). In Zhang and Niknejad, (2021), an absolute spin sensitivity of 6.1×10^8 spins/$\sqrt{\text{Hz}}$ for an on-chip EPR spectrometer operating at 14 GHz is stated, which however is not comparable with the sensitivities reported here. The reason for that is the different definition of the SNR in this work, which has also been used in Matheoud et al. (2017). To estimate this number, the SNR was calculated from the signal amplitude of an EPR spectrum of BDPA while the noise was obtained from a power spectral density (PSD) measurement at the modulation frequency of 50 kHz. We, however, calculated the SNR using the EPR spectrum only, which has been done in earlier works (Boero et al., 2003; Yalçin and Boero, 2008; Anders et al., 2012a; Handwerker et al., 2016; Chu et al., 2018). Since the PSD noise is usually better than the RMS noise of an EPR spectrum, the spin sensitivity values obtained with the PSD are usually lower.

https://doi.org/10.5194/mr-2021-40
Preprint. Discussion started: 3 May 2021

Open Access MAGNETIC RESONANCE Discussions

Table 1: SNR for CW-EPRoC and RS-EPRoC methods.

Method	Bias current, mA	B_1, µT	No. of averages	Modulation rate, THz s^{-1}	SNR	Measurement time, s	Normalized SNR, s^{-1}
CW-EPRoC	5	27.0	1	0.5	22	30.0	4.0
RS-EPRoC	7	45.5	1.5 x 10^5	80.4	236	0.75	272.9

3.2 Analysis of the transient RS-EPRoC signal

RS-EPRoC time traces recorded using four different bias currents (5 mA, 9 mA, 14 mA, 18 mA) corresponding to B_1 values of 27 µT, 62 µT, 95 µT, and 118 µT are shown in Fig. 3. The RS-EPRoC time traces were simulated and fit using a solution of *Bloch*'s equations in the steady-state for sinusoidal modulation. For the simulation, *Biot-Savart*'s law and a square-root coil current model were used to calculate the B_1 magnitude, which cannot be analytically calculated from the bias current driving the EPRoC sensor (See Appendix for more information). The simulations were performed using the transient AM RS-EPRoC signals without deconvolution, and the asymmetry of the AM signals was considered by including the quality factor from Eq. (1) in the simulations. The relaxation times of BDPA, $T_1 = 110$ ns and $T_2 = 100$ ns, were taken from the literature (Goldsborough et al., 1960; Mitchell et al., 2011b) and are required for the RS simulations. A thorough description of the simulations is given in the Appendix.

In Fig. 4, the signal intensities of CW- and RS-EPRoC measurements are compared as a function of B_1, demonstrating the saturation behavior of the BDPA-benzene complex observed via CW- and RS-EPRoC with rates of $\alpha =$ 80.4 THz s^{-1}, 201.1 THz s^{-1} and 402.1 THz s^{-1}. The CW- and RS-EPRoC signal increases with increasing B_1, as expected, and saturation is observed at higher values of B_1 for RS- compared to CW-EPRoC experiments. Increasing α leads to a linear regime that extends over several tens of µT, thus allowing the use of B_1 values beyond the relaxation-determined limit. Samples with slow relaxation rates especially benefit from the RS technique due to the signal saturation that is observed at low MW powers when using CW methods.

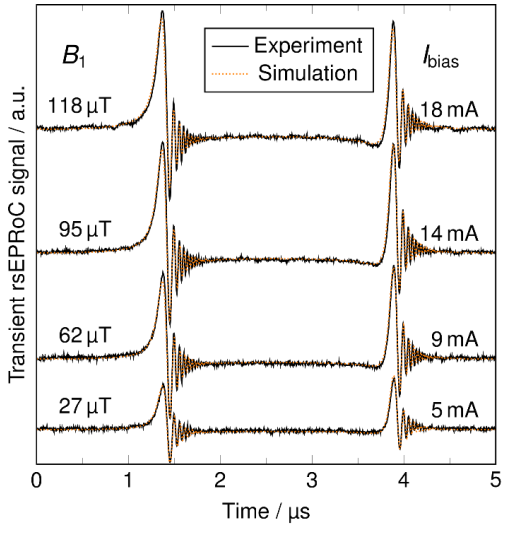

Figure 3: RS-EPRoC time traces (black) recorded using four different bias current values that correspond to four different B_1 magnitudes at a scan rate of 80 THz/s. The spin system passes through resonance twice during each period of the modulation of the MW frequency, see Eq. (5) and (6). The simulations (orange) of the transient acquired data are in good agreement with the experiment.

https://doi.org/10.5194/mr-2021-40
Preprint. Discussion started: 3 May 2021

Open Access MAGNETIC RESONANCE Discussions

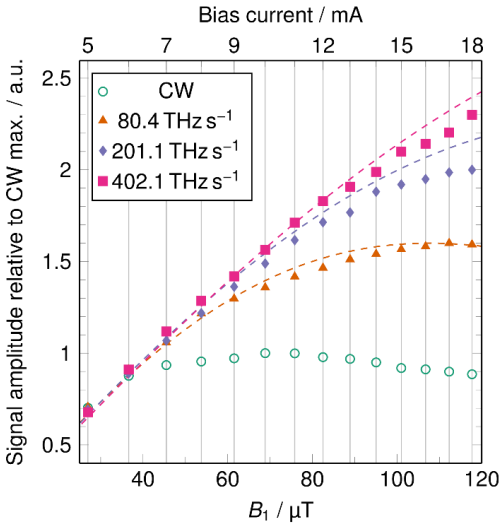

Figure 4: Signal amplitudes of CW-EPRoC (○) and RS-EPRoC for three scan rates (80.4 THz/s, ▲, 201.1 THz/s, ♦, and 402.1 THz/s, ■) as a function of bias current (x-axis, top) and corresponding B_1 magnitudes (x-axis, bottom). The dashed lines are simulations of the RS signals.

Finally, it is necessary to explore the theoretical limits of the RS-EPRoC technique. Figure 5 shows the simulated signal amplitudes of the deconvolved of transient RS-EPRoC signals as a function of both B_1 and scan rate, α. The scan rate was increased by increasing scan width while maintaining a constant scan frequency (200 kHz) to ensure that all oscillations have decayed within a single scan period (half-cycle) when considering T_1 and T_2^* on the order of 100 ns. The signal amplitudes were normalized to the global maximum of all signals resulting from the simulations to probe the limits of the RS-EPRoC technique with respect to SNR. This analysis extends the rapid scan technique far beyond what is possible with field-swept RS-EPR to encompass a regime that is only accessible via frequency-swept RS-EPR, which has now been implemented with RS-EPRoC. From this simulation, an improvement of the signal amplitude by a factor of about 5 is may be achieved compared to this work.

From the simulations, it was determined that simultaneously increasing both B_1 and α yields an increase in relative signal amplitude (yellow region in Fig. 5). For a constant B_1, an optimal scan rate, α, may be achieved that maximizes relative signal intensity without saturation; however, increasing the scan rate when the signal is unsaturated does not increase the signal intensity unless B_1 is similarly increased. Likewise, for a constant scan rate, α, an optimal B_1 may similarly be achieved that maximizes relative signal intensity without saturation, but additional increases in B_1 strength without an accompanying increase in scan rate lead to saturation and a decrease in signal intensity via power-dependent broadening. Thus, only an increase of both B_1 and scan rate will increase the relative signal amplitude in RS experiments, and this principle will guide further development of RS-EPRoC designs.

In these experiments, the available B_1 as indicated by the dashed rectangle in Fig. 5 is limited due to heating of the passively cooled EPRoC detector. If the EPRoC sensor was actively cooled, a B_1 of up to 250 µT (~factor of two) is possible with this generation of the EPRoC. In future EPRoC generations with a smaller coil diameter of 100 µm, the B_1 magnitude may be increased by an additional another factor of two. With the usage of other fabrication techniques than complimentary metal-oxide semiconductor (CMOS), such as BiCMOS and InGaAs, the total B_1 gain can be increased by another factor 10x compared to the current generation, resulting in absolute B_1 magnitudes of about 1 mT.

https://doi.org/10.5194/mr-2021-40
Preprint. Discussion started: 3 May 2021

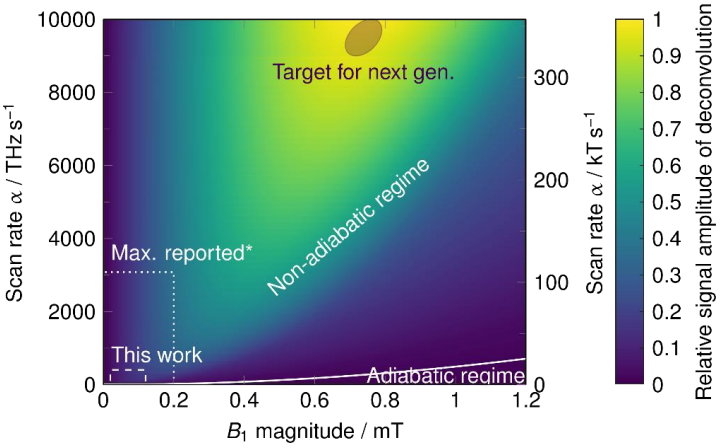

Figure 5: Relative simulated signal amplitude of the deconvolved RS signal as a function of both B_1 and scan rate α for BDPA. The solid line defines the adiabatic and non-adiabatic regions (Eq. (3) and (4)). The relaxation times were set to $T_1 = 110$ ns and $T_2^* = 100$ ns. The simulation was performed with a constant RS frequency (200 kHz) and increasing scan width (Eq. (6)). The two outlined rectangular regions (dashes) represent the accessible area for the current work as well as that of a study using field-swept RS-EPR where the maximum scan rate[*,3] was reported (Mitchell et al., 2011b). The ellipse shows the target region for the next-gen. EPRoC where the maximum signal is obtained. An improvement of the signal amplitude by a factor of about 5 is expected.

The scan rate may be increased by either extending the scan width, which decreases the time spent on resonance, or by using faster repetition rates, which increases the number of full frequency sweeps per unit time. The number of sweeps per unit time; however, is limited by the effective transverse relaxation time T_2^* (Tseytlin, 2017) given by the expression,

$$\frac{1}{f_{\mathrm{m}}} > N \cdot T_2^* \tag{7}$$

with N being in the range of 3 to 5, depending on the amount of acceptable line broadening introduced by Fourier deconvolution. This limit details the requirement that the RS signal oscillations or "wiggles" must have decayed completely before the next scan cycle is recorded (Fig. 2a).

Currently, the scan rate is not limited by the EPRoC array and its PLL, but by the signal generator supplying the PLL reference frequency. Commercially available analog signal generators, such as the Rohde & Schwarz SMB100B, may improve the scan rate ($\Delta f_{\mathrm{m,max}} = 160$ MHz (sweep width 11.4 mT), (2.5x) and $f_{\mathrm{m,max}} = 10$ MHz (10x)). However, as described by Eq. (7) the transverse relaxation time limits the usage of such high modulation frequencies. Additionally, the bandwidth of the PLL limits the modulation frequency to about 5 MHz, such that an improvement of the scan rate of a factor of 5 is realistic. The next-generation EPRoC with on-chip PLLs and higher bandwidths of up to 80 MHz is currently in development and will be capable of delivering scan rates of up to 10^4 THz/s via scan widths of more than 2.4 GHz (85.6 mT) and repetition rates of 2 MHz or more. Due to larger bandwidth of the PLL and a different PLL design where the FM signal may be extracted without filtering, the FM signal may additionally be used for data analysis exploiting the advantage of the array giving access to a larger sample volume and hence increased concentration sensitivity.

4 Conclusions

In this work non-adiabatic RS-EPRoC experiments are demonstrated, where an improvement in SNR of almost two orders of magnitude was achieved compared to CW-EPRoC. This in turn may improve the absolute spin and concentration sensitivity of EPRoC at 14 GHz to about 6×10^7 spins/$\sqrt{\mathrm{Hz}}$ and 3.6 nM/$\sqrt{\mathrm{Hz}}$, respectively. Additionally, we confirm that in RS-EPRoC

[3] The fastest scan rate currently reported for a frequency-swept high field/high frequency RS-EPR experiment was 267000 THz s^{-1} (Laguta et al., 2018) and is far beyond the limits of this plot.

https://doi.org/10.5194/mr-2021-40
Preprint. Discussion started: 3 May 2021

Open Access MAGNETIC RESONANCE Discussions

the RS signal is less prone to B_1 field saturation, similar to field-swept RS-EPR, and remains in the linear B_1 regime up to 90 µT for BDPA at the fastest scan rate investigated (402.1 THz/s).

Due to the larger frequency sweep width of the EPRoC array compared to field-swept RS-EPR it may be possible to use the EPRoC for sweep widths of up to 2.4 GHz (86 mT) or more. This increased width will extend RS-EPR spectroscopy to transition metal ions and other solid-state EPR spectra.

The ability to use small permanent magnets via frequency swept RS-EPR, coupled with its small size and power consumption, makes EPRoC applications very flexible. The EPRoC may be integrated into various complex and harsh sample environments enabling in situ and operando EPR measurements that have previously been inaccessible. This includes hand-held devices for *in-the-field* multiline fingerprinting applications in chemistry, medicine, biology, material science, and physics.

Appendices

Appendix A: Fourier deconvolution

The *Fourier* deconvolution procedure was published in detail in references (Joshi et al., 2005b; Tseitlin et al., 2011a; Tseytlin, 2017) and is briefly summarized here. To obtain the EPR spectrum, the RS signals must be *Fourier* deconvolved from the frequency spectrum of the MW excitation. Assuming a linear response $r(t)$ of the spin system under the influence of the excitation $d(t)$ and B_1 small enough to avoid saturation, we obtain:

$$r(t) = (h * d)(t) = \int_{-\infty}^{\infty} h(\tau) d(t-\tau) \mathrm{d}\tau \tag{8}$$

where $h(t)$ is the impulse response of the spin system (often referred to as "wiggles"), and $*$ denotes the convolution operator. The driving function (Tseitlin et al., 2011a) for the RS modulation, $d(t)$, is then defined as:

$$d(t) = \exp\left(i \int_0^t \omega(\tau) \mathrm{d}\tau\right) \tag{9}$$

In the frequency domain, the convolution in Eq. (8) becomes a multiplication:

$$R(\omega) = H(\omega) D(\omega) \tag{10}$$

where $R(\omega)$, $H(\omega)$, and $D(\omega)$ are the *Fourier* transforms of $r(t)$, $h(t)$, and $d(t)$, respectively. Thus, the EPR spectrum can be obtained in the frequency domain by a division as:

$$H(\omega) = R(\omega)/D(\omega) \tag{11}$$

The algorithm of the deconvolution procedure is as follows: The zero-padded transient baseline-corrected RS signal is *Fourier* transformed with a *Welch* apodization window (Welch, 1967). The excitation function is calculated assuming a sinusoidal frequency scan, numerically integrated, zero-padded and *Fourier* transformed with the same *Welch* apodization window. According to Eq. (11), the EPR spectrum containing both real and imaginary components of the complex susceptibility is obtained by the division of both *Fourier* transforms. The zero-padding function improves frequency resolution while the apodization window avoids sharp transitions to zero when zero-padding which would result in spikes in the *Fourier* transforms.

Appendix B: Bandwidth of the RS-EPRoC signal and its relation to the PLL bandwidth

The bandwidth of an RS-EPR signal for a single *Lorentzian* may be calculated from the scan rate α in Hz/s and the effective transverse relaxation time T_2^* (Mitchell et al., 2012),

$$\mathrm{BW}_{\mathrm{signal}} \approx N \alpha T_2^* \tag{12}$$

https://doi.org/10.5194/mr-2021-40
Preprint. Discussion started: 3 May 2021


Open Access MAGNETIC RESONANCE Discussions

where N is a parameter that describes the acceptable line shape broadening and is usually between 3 and 5. Since the resonance is passed twice in one RS cycle, only half of the available bandwidth of any detection system is available for the signal present in each half cycle, such that the BW of the detection system $\mathrm{BW}_{\mathrm{detection}}$ should be twice as large as the signal bandwidth as

$$\mathrm{BW}_{\mathrm{detection}} \geq 2N\alpha T_2^* \tag{13}$$

In ref. Mitchell et al. (2012), relation (13) was used to determine the quality factor needed for detection of an undistorted RS-EPR signal. Concerning the EPRoC, the bandwidth of the PLL, about 10 MHz, limits the bandwidth of the FM signal to about 5 MHz. Using a conservative estimate for $N = 5$, and a T_2^* of 110 ns, the signal bandwidth needed for an undistorted FM signal is about 80 MHz. Since the available bandwidth is much less than the required signal bandwidth, the FM signal was not considered in these experiments.

Appendix C: Digital post-processing of the EPRoC spectra

Both, CW- and RS-EPRoC spectra are digitally filtered with a moving average, 2nd order *Savitzky-Golay* filter. The filter window is adjusted such that the linewidth is broadened by less than 5%. For CW data, the effective acquisition time is calculated from the number of data points of the sweep, N_{points}, and the time constant of the lock-in amplifier, τ_{LIA}, as

$$T_{\mathrm{acq,cw}} = 3\, N_{\mathrm{points}} \cdot \tau_{\mathrm{LIA}} \tag{14}$$

A factor of 3 is introduced to take into account the rearm time of the lock-in amplifier required to achieve 99.9 % of the maximum signal intensity. For RS experiments, the effective acquisition time is calculated using the number of averages, N_{avg}, and both the number, N_{fc}, and the period, T_{fc}, of all RS cycles present in the signal acquisition, respectively, as

$$T_{\mathrm{acq,rs}} = N_{\mathrm{avg}} N_{\mathrm{fc}} T_{\mathrm{fc}} \tag{15}$$

The signal amplitude of the CW measurements is defined as the peak-to-peak amplitude of the AM signal. The root-mean-square (rms) noise is determined from the baseline regions of the spectrum (see Fig. 2b). For both CW- and RS-EPRoC measurements, ~61 % of the data points were used for calculation of the rms noise. The SNR is calculated as the ratio of the signal amplitude to the rms noise. The signal amplitude of the deconvolved RS-EPRoC spectrum is defined as the maximum value of the imaginary part of the deconvolved RS spectrum. The rms noise is calculated as for the CW measurements from the baseline regions of the spectrum. The SNR is calculated as the ratio of the signal amplitude to the rms noise. For the saturation analysis, the signal amplitude of the RS measurements is defined as the peak-to-peak amplitude of the transient RS signals since a deconvolution of the highest scan rate was not possible due to overlapping signals.
To compare the signal amplitudes of different methods and scan rates, the relative signal amplitude is used.

Appendix D: Fit parameters for Figure 2

The *Lorentzian* peak-to-peak linewidth of the fit of the deconvolved RS-EPRoC spectrum is 1.98 MHz (0.071 mT). The fit parameters of the CW-EPRoC spectrum are: *Lorentzian* peak-to-peak linewidth: 2.42 MHz (0.086 mT), $Q_{\mathrm{coil}} = 3.54$ as defined in Eq. (1). The measurement parameters of the CW spectrum are $f_{\mathrm{m}} = 100$ kHz; $\Delta f_{\mathrm{m,pp}} = 0.768$ MHz (0.028 mT), lock-in time constant, 10 ms and filter order, 24 dB.

Appendix E: Simulation of transient RS-EPR signals

All simulations of transient RS-EPR signals were performed by numerically solving the *Bloch* equations (Tseitlin et al., 2013; Stoll and Schweiger, 2006) in the steady state using *Easyspin*'s *blochsteady* function. A spin-1/2 system with a g-value of

https://doi.org/10.5194/mr-2021-40
Preprint. Discussion started: 3 May 2021

Open Access MAGNETIC RESONANCE Discussions

2.003, a *Lorentzian* line shape, and relaxation times $T_1 = 110$ ns and $T_2 = 100$ ns were assumed based on previous reports for BDPA (Goldsborough et al., 1960; Mitchell et al., 2011b).

1 Simulation of the transient RS-EPRoC signals to obtain B_1 magnitude

Since the range of the B_1 magnitude of the EPRoC is not precisely known and cannot be measured by *Rabi* oscillations due to the limited bandwidth of the PLL, 14 transient AM RS signals were recorded with increasing bias current and simulated as described in Appendix E without *Kramers-Kronig* manipulation and subsequent deconvolution. Thus, the lineshape asymmetry expected from Eq. (2) was also considered. To convert the bias current to a B_1 magnitude, a two-parameter square-root model of the current in the coil, I_{coil}, taking the curvature of the coil current at low bias current into consideration, was assumed as

$$I_{\mathrm{coil}} = a + b\sqrt{I_{bias}} \tag{16}$$

From this, the B_1 magnitude, as seen in Fig. E1, was calculated assuming a circular single turn inductor with a radius, R, of 100 µm using *Biot-Savart*'s law as

$$B_1 = \frac{1}{2}\,\mu_0 \frac{I_{\mathrm{coil}}}{2R} = \frac{1}{2}\,\mu_0 \frac{a+b\sqrt{I_{bias}}}{2R} \tag{17}$$

where μ_0 is the vacuum permeability. The factor of ½ takes into account that only half of the B_1 field is available for microwave excitation due to the two counter-rotating microwave fields in the rotating frame.

For the simulation of the AM RS-EPRoC signals, three global parameters were slightly varied for all transient RS signals - the parameters a and b and the quality factor Q of the VCO from Eq. (1).

2 Simulation of the RS-EPR signal amplitude as a function of B_1 and scan rate

For each point in Fig. 5, a complex transient RS-EPR signal containing both dispersion and absorption was simulated as described in Appendix E and subsequently deconvolved. From each deconvolution, the signal amplitude, which is the maximum of the absorption signal, was extracted. The obtained values were normalized to the global maximum of all the signal amplitudes obtained in order to form a relative comparison.

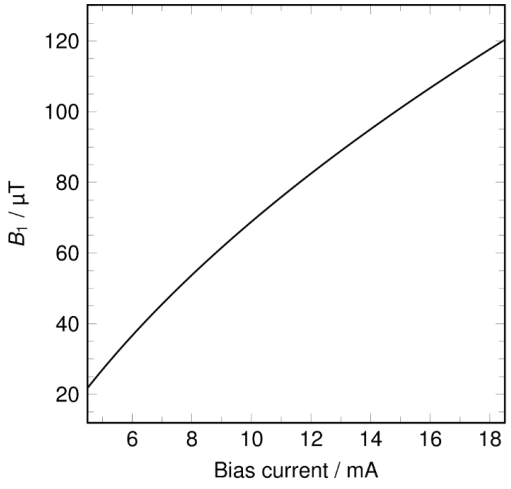

Figure E1: B_1 magnitude obtained by the square-root model of the bias current used throughout the EPRoC experiments reported in this manuscript.

https://doi.org/10.5194/mr-2021-40
Preprint. Discussion started: 3 May 2021

Open Access MAGNETIC RESONANCE Discussions

Appendix F: Determination of sample volume and mass

The sample volume was approximated using multiple photographs of the sample as shown in Fig. 1c while varying the light present to differentiate shadows from the sample material. To calculate the sample volume, a cuboid was assumed. The planar dimensions of the cuboid were determined from the shape of the sample in the photograph while height was determined using its shadow on the chip. In this way, the sample volume might be overestimated. The density of the BDPA-benzene complex is 1.220 g/cm^3 (Azuma et al., 1994). From the volume and the density, the sample mass was calculated.

Simulation and data processing availability

All programming used for data analysis, simulation, and processing is available from the authors on request.

Data availability

The data that support the findings of this study are available from the corresponding authors upon request.

Author contribution

SK, BN, AS and KL defined the goals of the research and designed the experiments. SK performed all EPR experiments, data processing, and simulations. AC and JA developed and assembled the EPR-on-a-Chip spectrometer. SK, JM and BN evaluated the results of the experiments and wrote the manuscript. KD advised the authors at all stages of the research and authoring of the manuscript.The paper was revised by all authors.

Competing interests

The authors declare that they have no conflict of interest.

Acknowledgements

We are grateful to Jannik Möser and Jason Sidabras for experimental support and for helpful discussions. This work has been supported by the Bundesministerium für Bildung und Forschung under contract number 01186916/1 (EPRoC) and by the HEMF (Helmholtz Energy Materials Foundry) infrastructure funded by the Helmholtz association (HGF). B.N. acknowledges the financial support from the DFG (project numbers 410866378 and 410866565).

References

Anders, J. and Lips, K.: MR to go, Journal of Magnetic Resonance, 306, 118–123, https://doi.org/10.1016/j.jmr.2019.07.007, 2019.

Anders, J., Angerhofer, A., and Boero, G.: K-band single-chip electron spin resonance detector, Journal of Magnetic Resonance, 217, 19–26, https://doi.org/10.1016/j.jmr.2012.02.003, 2012a.

Anders, J., Ortmanns, M., and Boero, G.: Noise in frequency-sensitive ESR detectors, IFAC Proceedings Volumes, 45, 451–456, https://doi.org/10.3182/20120215-3-AT-3016.00079, 2012b.

Azuma, N., Ozawa, T., and Yamauchi, J.: Molecular and Crystal Structures of Complexes of Stable Free Radical BDPA with Benzene and Acetone, BCSJ, 67, 31–38, https://doi.org/10.1246/bcsj.67.31, 1994.

https://doi.org/10.5194/mr-2021-40
Preprint. Discussion started: 3 May 2021

Open Access MAGNETIC RESONANCE Discussions

Boero, G., Bouterfas, M., Massin, C., Vincent, F., Besse, P.-A., Popovic, R. S., and Schweiger, A.: Electron-spin resonance probe based on a 100 µm planar microcoil, Review of Scientific Instruments, 74, 4794–4798, https://doi.org/10.1063/1.1621064, 2003.

Brodsky, M. H. and Title, R. S.: Electron Spin Resonance in Amorphous Silicon, Germanium, and Silicon Carbide, Phys. Rev. Lett., 23, 581–585, https://doi.org/10.1103/PhysRevLett.23.581, 1969.

Chu, A., Schlecker, B., Handwerker, J., Künstner, S., Ortmanns, M., Lips, K., and Anders, J.: VCO-based ESR-on-a-chip as a tool for low-cost, high-sensitivity food quality control, in: 2017 IEEE Biomedical Circuits and Systems Conference (BioCAS), 2017 IEEE Biomedical Circuits and Systems Conference (BioCAS), Torino, Italy, 1–4, https://doi.org/10.1109/BIOCAS.2017.8325172, 2017.

Chu, A., Schlecker, B., Lips, K., Ortmanns, M., and Anders, J.: An 8-channel 13GHz ESR-on-a-Chip injection-locked VCO-array achieving 200µM-concentration sensitivity, in: 2018 IEEE International Solid - State Circuits Conference - (ISSCC), 2018 IEEE International Solid-State Circuits Conference (ISSCC), San Francisco, CA, 354–356, https://doi.org/10.1109/ISSCC.2018.8310330, 2018.

Chu, A., Schlecker, B., Kern, M., Goodsell, J. L., Angerhofer, A., Lips, K., and Anders, J.: On the modeling of amplitude-sensitive ESR detection using VCO-based ESR-on-a-chip detectors, in preparation, 2021.

Eaton, G. R. and Eaton, S. S.: Rapid-Scan Electron Paramagnetic Resonance, in: eMagRes, edited by: Harris, R. K. and Wasylishen, R., John Wiley & Sons, Ltd, Chichester, UK, 1529–1542, https://doi.org/10.1002/9780470034590.emrstm1522, 2016.

Eaton, G. R., Eaton, S. S., Barr, D. P., and Weber, R. T.: Quantitative EPR, Springer Vienna, Vienna, Austria, https://doi.org/10.1007/978-3-211-92948-3, 2010.

Goldsborough, J. P., Mandel, M., and Pake, G. E.: Influence of Exchange Interaction on Paramagnetic Relaxation Times, Phys. Rev. Lett., 4, 13–15, https://doi.org/10.1103/PhysRevLett.4.13, 1960.

Gualco, G., Anders, J., Sienkiewicz, A., Alberti, S., Forró, L., and Boero, G.: Cryogenic single-chip electron spin resonance detector, Journal of Magnetic Resonance, 247, 96–103, https://doi.org/10.1016/j.jmr.2014.08.013, 2014.

Handwerker, J., Schlecker, B., Wachter, U., Radermacher, P., Ortmanns, M., and Anders, J.: A 14GHz battery-operated point-of-care ESR spectrometer based on a 0.13µm CMOS ASIC, in: 2016 IEEE International Solid-State Circuits Conference (ISSCC), 2016 IEEE International Solid-State Circuits Conference (ISSCC), San Francisco, CA, USA, 476–477, https://doi.org/10.1109/ISSCC.2016.7418114, 2016.

Hyde, J. S., Strangeway, R. A., Camenisch, T. G., Ratke, J. J., and Froncisz, W.: W-band frequency-swept EPR, Journal of Magnetic Resonance, 205, 93–101, https://doi.org/10.1016/j.jmr.2010.04.005, 2010.

Joshi, J. P., Eaton, G. R., and Eaton, S. S.: Impact of resonator on direct-detected rapid-scan EPR at 9.8 GHz, Appl. Magn. Reson., 28, 239–249, https://doi.org/10.1007/BF03166759, 2005a.

Joshi, J. P., Ballard, J. R., Rinard, G. A., Quine, R. W., Eaton, S. S., and Eaton, G. R.: Rapid-scan EPR with triangular scans and fourier deconvolution to recover the slow-scan spectrum, Journal of Magnetic Resonance, 175, 44–51, https://doi.org/10.1016/j.jmr.2005.03.013, 2005b.

Kittell, A. W., Camenisch, T. G., Ratke, J. J., Sidabras, J. W., and Hyde, J. S.: Detection of undistorted continuous wave (CW) electron paramagnetic resonance (EPR) spectra with non-adiabatic rapid sweep (NARS) of the magnetic field, Journal of Magnetic Resonance, 211, 228–233, https://doi.org/10.1016/j.jmr.2011.06.004, 2011.

Laguta, O., Tuček, M., van Slageren, J., and Neugebauer, P.: Multi-frequency rapid-scan HFEPR, Journal of Magnetic Resonance, 296, 138–142, https://doi.org/10.1016/j.jmr.2018.09.005, 2018.

Matheoud, A. V., Gualco, G., Jeong, M., Zivkovic, I., Brugger, J., Rønnow, H. M., Anders, J., and Boero, G.: Single-chip electron spin resonance detectors operating at 50 GHz, 92 GHz, and 146 GHz, Journal of Magnetic Resonance, 278, 113–121, https://doi.org/10.1016/j.jmr.2017.03.013, 2017.

Matheoud, A. V., Sahin, N., and Boero, G.: A single chip electron spin resonance detector based on a single high electron mobility transistor, Journal of Magnetic Resonance, 294, 59–70, https://doi.org/10.1016/j.jmr.2018.07.002, 2018.

https://doi.org/10.5194/mr-2021-40
Preprint. Discussion started: 3 May 2021

Open Access MAGNETIC RESONANCE Discussions

Meyer, V., Eaton, S. S., and Eaton, G. R.: X-band Electron Spin Relaxation Times for Four Aromatic Radicals in Fluid Solution and Comparison with Other Organic Radicals, Appl. Magn. Reson., 45, 993–1007, https://doi.org/10.1007/s00723-014-0579-6, 2014.

Mitchell, D. G., Quine, R. W., Tseitlin, M., Meyer, V., Eaton, S. S., and Eaton, G. R.: Comparison of continuous wave, spin echo, and rapid scan EPR of irradiated fused quartz, Radiation Measurements, 46, 993–996, https://doi.org/10.1016/j.radmeas.2011.03.035, 2011a.

Mitchell, D. G., Quine, R. W., Tseitlin, M., Weber, R. T., Meyer, V., Avery, A., Eaton, S. S., and Eaton, G. R.: Electron Spin Relaxation and Heterogeneity of the 1:1 α,γ-Bisdiphenylene-β-phenylallyl (BDPA)/Benzene Complex, J. Phys. Chem. B, 115, 7986–7990, https://doi.org/10.1021/jp201978w, 2011b.

Mitchell, D. G., Quine, R. W., Tseitlin, M., Eaton, S. S., and Eaton, G. R.: X-band rapid-scan EPR of nitroxyl radicals, Journal of Magnetic Resonance, 214, 221–226, https://doi.org/10.1016/j.jmr.2011.11.007, 2012.

Mitchell, D. G., Rosen, G. M., Tseitlin, M., Symmes, B., Eaton, S. S., and Eaton, G. R.: Use of Rapid-Scan EPR to Improve Detection Sensitivity for Spin-Trapped Radicals, Biophysical Journal, 105, 338–342, https://doi.org/10.1016/j.bpj.2013.06.005, 2013a.

Mitchell, D. G., Tseitlin, M., Quine, R. W., Meyer, V., Newton, M. E., Schnegg, A., George, B., Eaton, S. S., and Eaton, G. R.: X-band rapid-scan EPR of samples with long electron spin relaxation times: a comparison of continuous wave, pulse and rapid-scan EPR, Molecular Physics, 111, 2664–2673, https://doi.org/10.1080/00268976.2013.792959, 2013b.

Möser, J., Lips, K., Tseytlin, M., Eaton, G. R., Eaton, S. S., and Schnegg, A.: Using rapid-scan EPR to improve the detection limit of quantitative EPR by more than one order of magnitude, Journal of Magnetic Resonance, 281, 17–25, https://doi.org/10.1016/j.jmr.2017.04.003, 2017.

Neese, F.: Quantum chemistry and EPR parameters, in: eMagRes, edited by: Harris, R. K. and Wasylishen, R. L., John Wiley & Sons, Ltd, Chichester, UK, 1–22, https://doi.org/10.1002/9780470034590.emrstm1505, 2017.

Pound, R. V. and Knight, W. D.: A Radiofrequency Spectrograph and Simple Magnetic-Field Meter, Rev. Sci. Instrum., 21, 219–225, https://doi.org/10.1063/1.1745537, 1950.

Powles, J. G.: The Adiabatic Fast Passage Experiment in Magnetic Resonance, Proc. Phys. Soc., 71, 497–500, https://doi.org/10.1088/0370-1328/71/3/424, 1958.

Schlecker, B., Chu, A., Handwerker, J., Künstner, S., Ortmanns, M., Lips, K., and Anders, J.: Live demonstration: A VCO-based point-of-care ESR spectrometer, in: 2017 IEEE SENSORS, 2017 IEEE SENSORS, Glasgow, 1–1, https://doi.org/10.1109/ICSENS.2017.8234031, 2017a.

Schlecker, B., Chu, A., Handwerker, J., Künstner, S., Ortmanns, M., Lips, K., and Anders, J.: VCO-based ESR-on-a-chip as a tool for low-cost, high-sensitivity point-of-care diagnostics, in: 2017 IEEE SENSORS, 2017 IEEE SENSORS, Glasgow, 1–3, https://doi.org/10.1109/ICSENS.2017.8233896, 2017b.

Stoll, S. and Schweiger, A.: EasySpin, a comprehensive software package for spectral simulation and analysis in EPR, Journal of Magnetic Resonance, 178, 42–55, https://doi.org/10.1016/j.jmr.2005.08.013, 2006.

Switala, L. E., Black, B. E., Mercovich, C. A., Seshadri, A., and Hornak, J. P.: An electron paramagnetic resonance mobile universal surface explorer, Journal of Magnetic Resonance, 285, 18–25, https://doi.org/10.1016/j.jmr.2017.10.004, 2017.

Tseitlin, M., Quine, R. W., Rinard, G. A., Eaton, S. S., and Eaton, G. R.: Combining absorption and dispersion signals to improve signal-to-noise for rapid-scan EPR imaging, Journal of Magnetic Resonance, 203, 305–310, https://doi.org/10.1016/j.jmr.2010.01.013, 2010.

Tseitlin, M., Rinard, G. A., Quine, R. W., Eaton, S. S., and Eaton, G. R.: Deconvolution of sinusoidal rapid EPR scans, Journal of Magnetic Resonance, 208, 279–283, https://doi.org/10.1016/j.jmr.2010.11.015, 2011a.

Tseitlin, M., Rinard, G. A., Quine, R. W., Eaton, S. S., and Eaton, G. R.: Rapid frequency scan EPR, Journal of Magnetic Resonance, 211, 156–161, https://doi.org/10.1016/j.jmr.2011.05.006, 2011b.

Tseitlin, M., Eaton, G. R., and Eaton, S. S.: Computationally Efficient Steady-State Solution of the Bloch Equations for Rapid Sinusoidal Scans Based on Fourier Expansion in Harmonics of the Scan Frequency, Appl. Magn. Reson., 44, 1373–1379, https://doi.org/10.1007/s00723-013-0494-2, 2013.

https://doi.org/10.5194/mr-2021-40
Preprint. Discussion started: 3 May 2021

Open Access MAGNETIC RESONANCE Discussions

Tseytlin, M.: Full cycle rapid scan EPR deconvolution algorithm, Journal of Magnetic Resonance, 281, 272–278, https://doi.org/10.1016/j.jmr.2017.06.008, 2017.

Van Doorslaer, S. and Vinck, E.: The strength of EPR and ENDOR techniques in revealing structure–function relationships in metalloproteins, Phys. Chem. Chem. Phys., 9, 4620–4638, https://doi.org/10.1039/B701568B, 2007.

Villamena, F. A.: Chapter 5 - EPR Spin Trapping, in: Reactive Species Detection in Biology, edited by: Villamena, F. A., Elsevier, Boston, US, 163–202, https://doi.org/10.1016/B978-0-12-420017-3.00004-9, 2017.

Weger, M.: Passage Effects in Paramagnetic Resonance Experiments, The Bell System Technical Journal, 39, 1013–1112, https://doi.org/10.1002/j.1538-7305.1960.tb03951.x, 1960.

Welch, P.: The use of fast Fourier transform for the estimation of power spectra: A method based on time averaging over short, modified periodograms, IEEE Trans. Audio Electroacoust., 15, 70–73, https://doi.org/10.1109/TAU.1967.1161901, 1967.

Wolfson, H., Ahmad, R., Twig, Y., Blank, A., and Kuppusamy, P.: A hand-held EPR scanner for transcutaneous oximetry, in: Medical Imaging 2015: Biomedical Applications in Molecular, Structural, and Functional Imaging, Medical Imaging 2015: Biomedical Applications in Molecular, Structural, and Functional Imaging, 941706, https://doi.org/10.1117/12.2083864, 2015.

Yalçin, T. and Boero, G.: Single-chip detector for electron spin resonance spectroscopy, Rev. Sci. Instrum., 79, 094105, https://doi.org/10.1063/1.2969657, 2008.

Yu, Z., Liu, T., Elajaili, H., Rinard, G. A., Eaton, S. S., and Eaton, G. R.: Field-stepped direct detection electron paramagnetic resonance, Journal of Magnetic Resonance, 258, 58–64, https://doi.org/10.1016/j.jmr.2015.06.011, 2015.

Zgadzai, O., Twig, Y., Wolfson, H., Ahmad, R., Kuppusamy, P., and Blank, A.: Electron-Spin-Resonance Dipstick, Anal. Chem., 90, 7830–7836, https://doi.org/10.1021/acs.analchem.8b00917, 2018.

Zhang, L. and Niknejad, A. M.: An Ultrasensitive 14-GHz 1.12-mW EPR Spectrometer in 28-nm CMOS, IEEE Microw. Wireless Compon. Lett., 1–1, https://doi.org/10.1109/LMWC.2021.3060730, 2021.